

KINEMATIC ANALYSES OF THE HSÜEHSHAN RANGE, TAIWAN: A LARGE-SCALE POP-UP STRUCTURE

M. Brooks Clark and Donald M. Fisher
Department of Geosciences, Pennsylvania State University,
University Park

Chia-Yu Lu
Department of Geology, National Taiwan University, Taipei,
Taiwan, Republic of China

Chao-Hsia Chen
Central Geological Survey, Ministry of Economic Affairs,
Taipei, Taiwan, Republic of China

Abstract. The Hsüehshan Range, exposed in the northern and central Taiwan slate belt, is a fault-bounded structural high cored by biotite grade slates and metasandstones. Syntectonic overgrowths in pyrite pressure shadows indicate that much of the eastern Hsüehshan Range experienced coaxial strain histories and that finite strain magnitudes generally increase toward the hinterland. Near the eastern boundary of the Hsüehshan Range, however, pressure shadows record noncoaxial strain histories consistent with a top-to-the-east sense of shear along a steep NW dipping shear zone. This noncoaxiality is attributed to SE directed backthrusting on the Lishan fault, which separates the higher-grade, Eo-Oligocene rocks of the Hsüehshan Range from the lower-grade Miocene rocks of the Backbone Range. Because it is bounded to the east by the SE-vergent Lishan fault and to the west by a series of NW-vergent thrusts (e.g., the Chüchih fault), the Hsüehshan Range is envisaged as a pop-up structure. Strain magnitudes measured from pressure shadows in the coaxial part of the range are consistently lower than those predicted by steady state wedge models that assume all deformation is accommodated by penetrative strain. Departure from the model predictions is attributed primarily to strain localization along discrete fault surfaces (e.g., the Lishan fault). The Hsüehshan Range tapers in width to the south; thus the pop-up may be buried or die out to the south where the collision is younger.

INTRODUCTION

Taiwan, located on the boundary between the Eurasian and Philippine Sea plates, is the classic example of an active arc-continent collision and is a result of the ongoing collision between the Luzon island arc and the Asian continental margin (Figure 1). Because the Asian margin is oriented NE-SW and the Luzon island arc is oriented N-S, the NW vergence of the Philippine Sea plate relative to the Eurasian plate [Seno, 1977] results in an oblique collision which propagates southward at a rate of 90 km/m.y. [Suppe, 1981]. This obliquity results in a time-space equivalence, such that a distance of 90 km parallel to strike represents a time difference of 1 m.y. in the evolution

of the collision. Consequently, the Taiwan mountain belt is approximately 4 m.y. older in the north than in the south.

In spite of this north to south age difference, the mountain belt has a constant width for nearly 150 km along strike, an observation which Suppe [1981] attributed to a balance between the flux of material into the wedge by accretion and the flux of material out of the wedge due to erosion (i.e., steady state geometry). Dahlen and Barr [1989] used this steady state assumption as the basis for a kinematic model in which particles enter the wedge through the toe or base by accretion and underplating, respectively, and follow hyperbolic paths through the wedge until they are removed at the surface by erosion. Velocity gradients within the wedge result in penetrative strain, where the principal incremental strain axes are fixed and always parallel to the principal stress directions (i.e., isotropic material). Particle velocities within the wedge are a function of only the wedge geometry and fluxes at the boundaries. The kinematic model proposed by Dahlen and Barr [1989] predicts (1) a steep, SE dipping cleavage, (2) an up-dip extension direction, (3) a progressive increase in strain magnitudes from foreland to hinterland across the wedge, and (4) an increase in the maximum depth of burial and therefore metamorphic grade from foreland to hinterland [Barr and Dahlen, 1989; Barr et al., 1991].

Although there have been several studies of the thermal history and structure of Taiwan using apatite and zircon fission track [Liu, 1982, 1988; Hsieh, 1990], illite crystallinity [Chen, 1981, 1984], and surface heat flow [Lee and Cheng, 1986] data, there have been few detailed studies of the kinematics and strain histories, particularly in the highly deformed internal portions of the mountain belt. In this paper, we use syntectonic overgrowths in pyrite pressure shadows to quantify the kinematics of deformation in the Hsüehshan Range, a fault-bounded structural high exposing intermediate grade slates and metasandstones in northern and central Taiwan. Finite strain magnitudes are compared with the values predicted by the Dahlen and Barr [1989] model.

GEOLOGIC SETTING

The Taiwan orogenic belt consists of a variety of different rock types which provide a nearly complete record of the precollisional and syncollisional tectonic history of the region, including Eo-Oligocene rifting and opening of the South China Sea [Teng et al., 1991], forearc basin sedimentation [Lundberg and Dorsey, 1988], accretion of the arc and forearc basin, and crustal shortening of 160-200 km [Suppe, 1981]. In general, Taiwan is divided into four major N-S trending tectonostratigraphic terranes based on differences in age, metamorphic grade, and structural style. From west to east, these terranes include the Coastal Plain, the Western Foothills, the Central Range, and the Coast Range (Figure 1). With the exception of the Coast Range, which represents the accreted volcanic arc and forearc basin, age, metamorphic grade, and deformation intensity all tend to increase from foreland to hinterland (west to east) across the island. The Western Foothills represents a fold-thrust belt and is characterized by NW-vergent structures [Suppe, 1980]. Rocks range in age from Oligocene to Pliocene and are essentially nonmetamorphosed.

The Central Range consists of a highly deformed cover sequence of prehnite-pumpellyite to lower greenschist facies slates and metasandstones (slate belt) in the west, and a

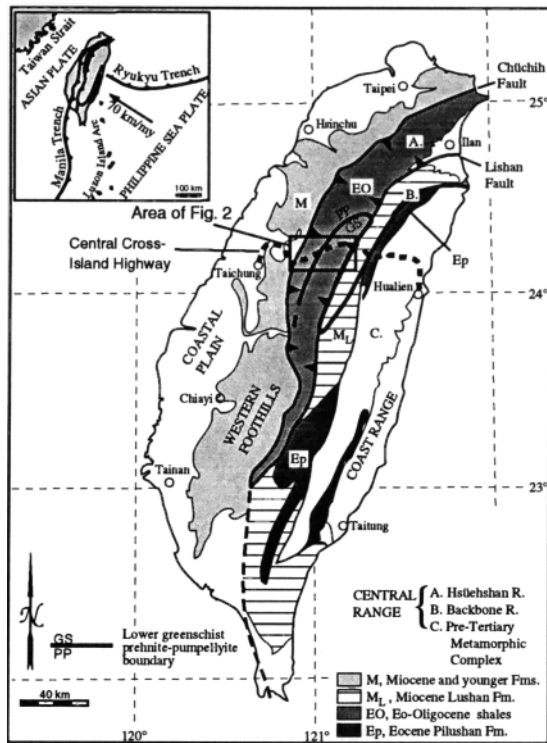


Fig. 1. Map showing the tectonic setting of Taiwan (inset), and map of Taiwan showing the major tectonostratigraphic units. The bold line shows the prehnite-pumpellyite/lower greenschist facies boundary (PP/GS) determined by Chen et al. [1983]. Location of Figure 2 is shown by the box. Maps are after Chen [1984] and Ho [1986].

polydeformed pre-Tertiary metamorphic complex in the east (Figure 1). On the basis of differences in age and metamorphic grade, the slate belt is further divided into the Hsüehshan and Backbone ranges. The Backbone Range consists of Eocene and Miocene (Oligocene missing (?)) slates and minor interbedded sandstones (Figures 1 and 2), whereas the Hsüehshan Range consists of Eocene through Oligocene slates and metasandstones [Ho, 1975, 1988]. On its eastern boundary, the Hsüehshan Range is separated from the Backbone Range by the Lishan fault (previously mapped as a fault of unknown nature [Ho, 1975, 1988]), which juxtaposes the Eo-Oligocene rocks of the Hsüehshan Range against Miocene rocks of the western Backbone Range. On the west, the Hsüehshan Range is bounded by the Chüchih fault, a moderately SE dipping, NW-vergent thrust fault [Biq, 1971], which separates the Hsüehshan Range from the nonmetamorphosed, Miocene and younger rocks of the Western Foothills. The Hsüehshan Range is therefore a structural high. Exposure of these Eo-Oligocene rocks in the middle of the mountain belt reflects a departure from the overall increase in age toward the hinterland as predicted by the Dahlen and Barr [1989] kinematic model and as observed in southern Taiwan where the Hsüehshan Range is not exposed (Figure 1).

Based on fission track [Liu, 1982, 1988; Hsieh, 1990] and illite crystallinity [Chen, 1981, 1984] data, this age anomaly corresponds to a thermal anomaly. Metamorphic grade generally increases across the Hsüehshan Range from

prehnite-pumpellyite facies in the west to lower greenschist facies in the east [Chen, 1981, 1984; Chen et al., 1983], although a higher metamorphic grade in the core of the Tachien anticline is suggested by the presence of metamorphic biotite [Yen, 1973]. There is an abrupt drop in metamorphic grade across the Lishan fault, from low greenschist facies in the eastern Hsüehshan Range to prehnite-pumpellyite facies in the western Backbone Range [Chen, 1981, 1984; Chen et al., 1983; Hsieh, 1990] (see Figure 1, prehnite-pumpellyite/lower greenschist facies boundary). Thus the Lishan fault is an important structural contact because, in contrast to the regional trends of increasing age and metamorphic grade from west to east, there is a decrease in both age and metamorphic grade across this boundary; yet its nature and orientation are largely unknown because of poor exposure. Whereas several workers [Biq, 1971; Wu, 1978] have suggested that the Lishan fault is a major east dipping, west-vergent thrust, Teng et al. [1991] have more recently suggested that the Lishan fault initially developed as a west dipping normal fault during Paleogene rifting. Moreover, because of the absence of Oligocene sediments in the Backbone Range [Ho, 1975, 1988], Teng et al. [1991] propose that the Lishan fault acted as a growth fault with little sediment accumulation in the footwall (Backbone Range) and thick accumulation in the hanging wall (Hsüehshan Range).

To characterize the kinematics of the Hsüehshan Range and determine the nature of the Lishan fault, detailed mapping was conducted in the eastern Hsüehshan Range primarily along the Central Cross-Island Highway. Mapping also involved collecting numerous oriented samples for incremental strain analysis. The location of the field area is shown in Figure 2. In this study, we recognize three units: the Eocene Tachien Sandstone, the Eo-Oligocene Chiayang Formation, and the Miocene Lushan Formation, all of which are passive margin [Chen, 1979]. The Tachien Sandstone is a massive, coarse-grained, quartzo-feldspathic sandstone with minor slaty and carbonaceous interbeds, particularly near the top. This unit crops out in the western part of the field area in the core of a large anticline, herein referred to informally as the Tachien anticline, and has a total estimated thickness of 2700 m [Chen, 1979]. The Tachien Sandstone fines and thins upward and grades conformably into the overlying Chiayang Formation.

The Chiayang Formation is a thick, Eo-Oligocene massive sequence of black to tan slates and minor interbedded sandstones [Ho, 1975, 1988] which crops out on the eastern flank of the Hsüehshan Range. Chen [1979] estimates the total thickness of the Chiayang Formation to be of the order of 3000 m. The Lushan Formation, which crops out on the western flank of the Backbone Range, consists of fossiliferous slates, siltstones, and minor thin- and thick-bedded sandstones and is estimated to be as much as 5000 m thick [Chen, 1979]. The lack of fossils within the Chiayang Formation serves to distinguish it from the Lushan Formation, which contains abundant Miocene foraminifera [Ho, 1975, 1988] and shows evidence for extension prior to and during collision [Crespi, 1991].

STRUCTURAL GEOLOGY

Large-scale and Mesoscale Structures

The Tachien Sandstone and Chiayang Formation show drastically different structural styles. The Tachien Sandstone is

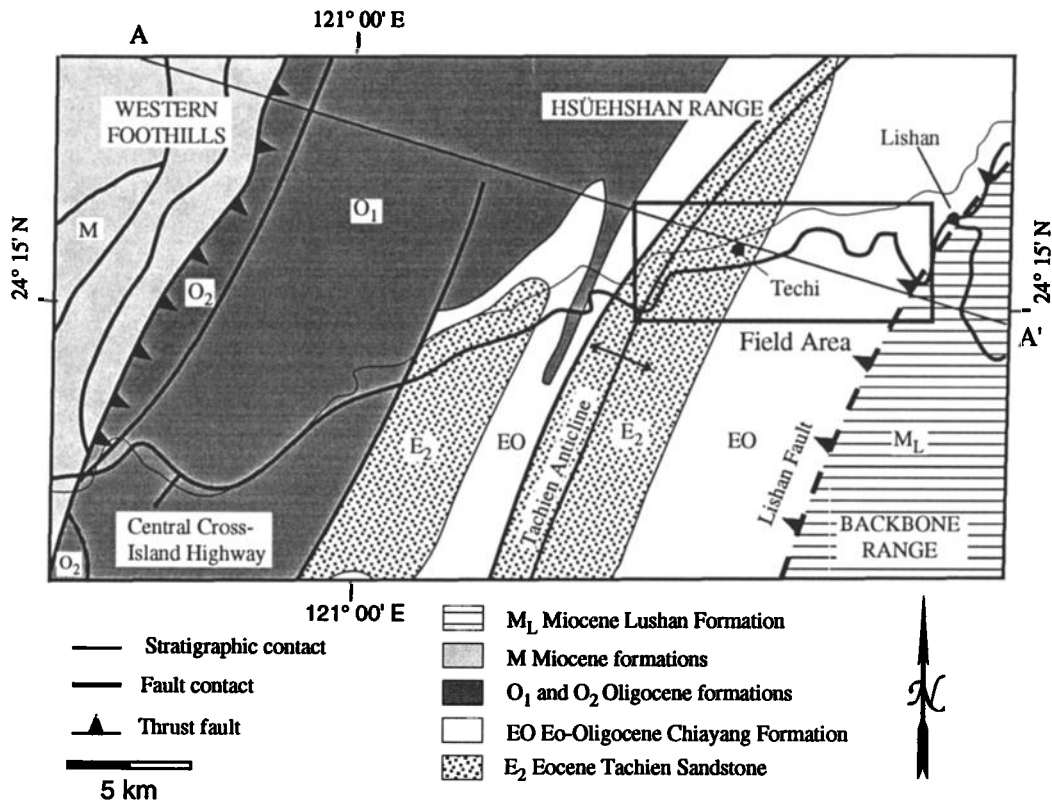


Fig. 2. Geologic map of the Central Range in the vicinity of the Central Cross-Island Highway. The Hsüehshan Range, which consists of the Eocene to Oligocene (E and EO) rocks, is flanked on either side by Miocene (M and M_L) rocks. The location of the field area (Figure 3) is shown by the box. Map is redrawn from the Geologic map of Taiwan [Ho, 1986].

folded into a large anticline (Figure 3), which exposes the lowest structural levels and the highest metamorphic grades anywhere in the Hsüehshan Range. Metamorphic biotite, recognized in the core of this anticline [Yen, 1973], disappears both to the east and west. To the east, biotite porphyroblasts decrease in grain size progressively further from the core of the anticline and disappear entirely. Because the samples have approximately the same mineralogic composition, the loss of biotite to the east is interpreted to represent an isograd (Figure 3) and not a result of changes in bulk composition. The biotite also disappears to the west on the opposing limb of the anticline [Tillman, 1991].

Folding of the Tachien Sandstone was accompanied by significant flexural slip, resulting in the formation of bedding-parallel faults, particularly on the southeast margin of the fold (Figure 3). These faults are restricted to slaty interbeds and consist of a fine-grained, carbonaceous fault gouge. Slickenlines are approximately downdip, perpendicular to the fold axis (02°/023°) and, together with the fabric within the fault, indicate a thrust sense of shear, consistent with flexural slip. Two sets of veins are recognized in the Tachien Sandstone, including an early set of quartz-chlorite-calcite (minor) veins indicating NNE-SSW extension (Figure 3) and a later set of bedding-parallel veins. The NNE-SSW extension veins are pre-folding and show evidence for deformation and recrystallization of quartz grains. The bedding-parallel veins may represent flexural slip faults.

The Chiayang Formation displays a steep, southeast dipping cleavage and an approximately updip stretching lineation (Figure 3). With the exception of minor folds, bedding also dips steeply to the southeast and ranges from being slightly shallower (<8°) than cleavage in the western part of this unit to being parallel (<1°) in the eastern part. Veins are rare in the Chiayang Formation, and where present, are strongly deformed with pinch and swell structures that indicate subvertical extension. Discrete fault surfaces are not commonly observed within the Chiayang Formation.

Microstructures

Slate samples from the eastern Hsüehshan Range generally have a well-developed slaty cleavage defined by the subparallel alignment of phyllosilicate and elongate quartz grains as well as the accumulation of layers of insoluble residue. Samples 90-86 and 90-88 from near the Lishan fault also have a poorly developed crenulation cleavage that dips moderately to the SE. Syntectonic overgrowths are common adjacent to quartz and framboidal pyrite grains. Overgrowths are also common on metamorphic biotite grains, indicating that the biotite predates the development of cleavage. In the next section, quartz-chlorite fibers in pyrite-type pressure shadows are used to quantify the incremental strain and progressive finite strain histories.

INCREMENTAL STRAIN ANALYSIS

Syntectonic fibers in pressure shadows record the relative displacements between initially adjacent points [Durney and Ramsay, 1973; Wickham, 1973] and can therefore be used to reconstruct the strain path followed by a deformed rock [Durney and Ramsay, 1973; Wickham, 1973; Ramsay and Huber, 1983; Beutner and Diegel, 1985; Ellis, 1986]. If the fibers are assumed to be parallel to the extension direction, then the elongation $\epsilon = \Delta l / l_0$ can be measured directly, where the original length l_0 is the radius of the pyrite, and the change in length Δl is the length of the fiber [Durney and Ramsay, 1973]. Alternatively, if no a priori assumption is made about the orientation of the extension direction, the displacements can be used to solve for both the orientation and magnitude of extension as described by Wickham [1973] for rigid fibers and by Ellis [1986] for deformable fibers.

In general, strain histories can be classified as being coaxial (irrotational), where each successive increment of strain is parallel to earlier increments, or noncoaxial (rotational), where successive increments are not parallel to earlier increments. Coaxial strain histories are characterized by pressure shadows with straight fibers (only the central fiber is straight if the fibers are deformable) (Figures 4a and 4b). Noncoaxial strain histories are characterized by pressure shadows with curved fibers (Figure 4c) and may reflect (1) rotation of the rock through a constant extension direction, (2) rotation of the extension direction relative to the rock, or (3) a component of simple shear.

Methods and Assumptions

In this paper, we use the Ellis [1986] method to quantify the cumulative incremental strain and progressive finite strain histories. This method assumes (1) antitaxial fiber growth, (2) plane strain deformation, and (3) deformable fibers. In virtually all previous incremental strain studies using quartz-chlorite overgrowths on a framboidal pyrite host, fiber growth has been demonstrated to be antitaxial [Durney and Ramsay, 1973; Gray and Durney, 1979; Ramsay and Huber, 1983; Beutner and Diegel, 1985; Ellis, 1986; Fisher, 1990; Fisher and Byrne, 1992]. In other words, the fibers grow from the matrix toward the host, and the youngest fiber segments are those closest to the pyrite. Antitaxial growth is further supported by two observations. First, in samples 90-86 and 90-88 which have a poorly developed crenulation cleavage, the fiber segment next to the pyrite is approximately parallel to the second cleavage, suggesting that these fibers are related to the crenulation cleavage. Because the crenulation cleavage is one of the last fabrics to develop in this rock, the fibers adjacent to the host must be the last to precipitate. Second, overgrowths on quartz grains are in optical continuity with the grain, and therefore growth is syntaxial (from the host toward the matrix). The curvature of these fibers is opposite that of the pyrite pressure shadows, again consistent with antitaxial growth next to pyrite.

To evaluate the validity the plane strain assumption, we consider the three-dimensional geometry of the pressure shadow by making two orthogonal thin sections, one parallel to cleavage (XY section), and one perpendicular to cleavage and parallel to the extension direction (XZ section). Viewed in XY sections, all samples except 90-95 have pressure shadows with approximately straight fibers parallel to the stretching lineation (X) (Figure 4a). The pressure shadow maintains a

constant width outward from the pyrite, and there are no fibers parallel to the intermediate principal stretch direction (Y). These observations suggest that there is no shortening or extension parallel to Y, consistent with plane strain deformation. Also, fibers are generally almost straight in XY sections, indicating that they do not curve into and out of the XZ sections. As an additional test to this assumption, we digitized fibers on both sides of individual pyrites (viewed in XZ sections). Fibers on either side of a pyrite give similar strain history curves.

Finally, we have chosen to use a deformable fiber technique primarily because pressure shadows viewed in XZ sections taper in width away from the pyrite suggesting that the pressure shadow has undergone shortening parallel to Z. In samples which record coaxial strain histories, typically only the central fiber is straight; all other fibers are asymptotic to the central fiber (Figure 4b). This geometry is characteristic of deformable fibers [Ellis, 1986]. In samples with straight fibers, we calculated the elongation by measuring the length of the central fiber and dividing by the radius of the pyrite. The data are reported as an average elongation for each sample (Table 1).

In samples with curved fibers, we digitized a single fiber from each pressure shadow, where the number of points used to represent the fiber geometry is inversely proportional to the radius of curvature of the fiber. A computer program was used to calculate the cumulative incremental and progressive finite strain histories for the sample; the strain histories are plotted on cumulative incremental strain and progressive finite strain history diagrams [Fisher, 1990; Fisher and Byrne, 1992]. Cumulative incremental strain history diagrams show the sum of the incremental elongations (ϵ) for the 1 through i th increment versus the orientation (ξ) of the i th increment, and progressive finite strain history diagrams show the finite elongation (E) versus orientation (Θ) as strain accumulates. Essentially, progressive finite strain diagrams reflect the shape and orientation of the finite strain ellipse. The orientation is measured relative to reference frame fixed within each thin section. In this paper, all measurements are reported with respect to S_1 cleavage, where counterclockwise angles are defined as positive. The present orientation of a fiber segment, however, does not necessarily reflect the orientation of the extension direction calculated for that segment for two reasons. First, the Ellis [1986] method assumes that fibers record pure shear displacement paths relative to the center of the pyrite framboid. These displacement paths are not necessarily parallel to the extension direction. Second, because fibers are assumed to be deformable, the length and orientation of older fiber segments change as successively younger increments of strain accumulate. To calculate the strain history, older fiber segments are progressively unstrained to restore them to their original length and orientation.

The cumulative incremental strain and progressive finite strain history curves (e.g., Figure 5) show several gray curves which represent strain histories recorded by individual fibers, as well as an average curve in black. The average curve is determined by calculating the average of the lower and upper endpoints for all curves ($\bar{\xi}_1, \bar{\epsilon}_1$) and ($\bar{\xi}_n, \bar{\epsilon}_n$), respectively. Each individual curve is normalized to the average of the endpoints using the equations

$$A_{ij} = A_{ij} - (A_{1j} - \bar{A}_1) \left[1 - \frac{(B_{ij} - B_{1j})}{(B_{nj} - B_{1j})} \right], \quad (1)$$

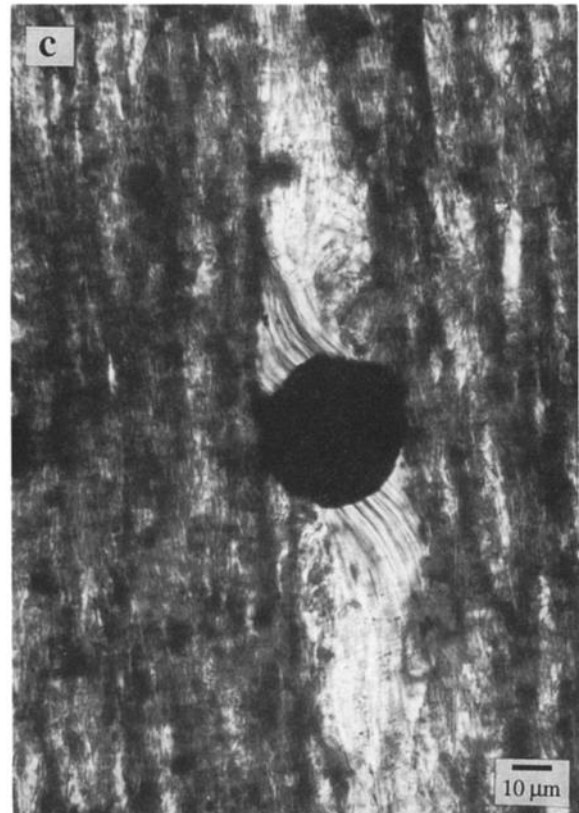
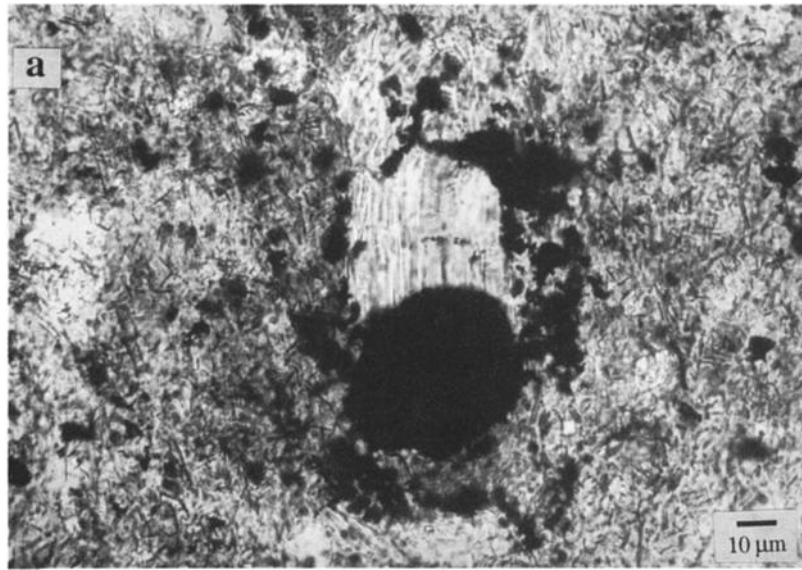


Fig. 4. (a) Photomicrograph of pressure shadow adjacent to framboidal pyrite grain in sample 90-88, viewed in XY section, looking toward the east. The orientation of the fibers is independent of the orientation of the growth interface suggesting displacement-controlled rather than face-controlled growth. Pressure shadows in this sample are noncoaxial in XZ sections (Figure 4c); thus the fibers curve in and out of the plane of the thin section when viewed parallel to cleavage. (b) Photomicrograph of pressure shadow in XZ section (viewed toward the northeast), indicating a coaxial strain history. Cleavage dips steeply to the southeast in the outcrop. Unlike the pressure shadow viewed in the XY section, only the

TABLE 1. Average Elongations Measured From Samples With Coaxial Strain Histories

Sample	Average Elongation, ϵ	Standard Deviation	Number of Measurements, n	Region
90-67	2.4	0.73	10	I
90-105	3.7	0.91	34	I
90-26	1.8	0.36	19	II
90-28	2.5	0.85	61	II
90-30	2.1	0.67	69	II
90-39	1.5	0.42	53	II
90-50a	2.1	0.29	16	II
90-51	1.9	0.34	30	II
90-53	2.1	0.29	11	II
90-54	2.5	0.13	2	II
90-61	2.5	0.38	12	II
90-64	1.9	0.32	26	II
90-65	1.4	0.36	23	II
90-72	1.3	0.26	24	II

to normalize to the lower endpoint ($\bar{\xi}_1, \bar{\epsilon}_1$), and

$$A_{ij} = A_{ij} - (A_{nj} - \bar{A}_n) \left[\frac{(B_{ij} - B_{1j})}{(B_{nj} - B_{1j})} \right] \quad (2)$$

to normalize to the upper endpoint ($\bar{\xi}_n, \bar{\epsilon}_n$), where A corresponds to ξ when B corresponds to ϵ and vice versa. The first subscript refers to points along the curve and ranges from 1 to n, where 1 is the lowermost point and n is the uppermost point. The second subscript, j, refers to the number of the curve being normalized. The term inside the brackets is a scaling factor so that the amount a point is shifted is inversely proportional to its distance from the endpoint. For example, when normalizing to the upper endpoint, the position of the lowermost point on the curve is not changed. The average curve is then calculated by choosing a value for ϵ and determining the corresponding value of ξ for each normalized curve. The ξ values are then averaged, and the previous step is repeated for a different value of ϵ . The average progressive finite strain history curve is calculated from the average incremental strain history curve.

Results

On the basis of differences in strain magnitudes and incremental strain histories, the field area can be divided into three regions. Samples from regions I and II have pressure shadows where the central fiber is straight (Figure 4b), reflecting a coaxial strain history. Region I includes two samples (90-67 and 90-105) from slate interbeds in the upper part of the Tachien Sandstone and is differentiated from region II because the pressure shadows in these samples record anomalously high finite strains (Table 1). We attribute these anomalously high strains to strain partitioning into slate interbeds within a more competent sandstone. The absence or poor development of cleavage in the sandstones suggests that

the elongations within massive sandstone beds are probably significantly less.

Region II includes 12 samples from within the Chiayang Formation (Figure 3 and Table 1). Finite strain magnitudes generally increase from west to east across region II, but drop off near the Lishan fault. Figure 6 shows a plot of elongation versus distance from the Lishan fault, perpendicular to regional strike. The solid line is the best fit line through nine points (solid squares) showing a gradual increase in strain magnitude toward the fault. The remaining three points in region II are located within 1 1/2 km of the fault and record anomalously low finite strains. Near the Lishan fault, shortening may be accommodated by volume loss or slip on the fault surface itself with less penetrative extension in the surrounding rocks.

Region III, located near the contact between the Hsüehshan and Backbone ranges, is characterized by pressure shadows that record noncoaxial strain histories in XZ sections (Figure 4c). Figure 4a shows a pressure shadow from the same sample viewed in the XY section. The apparent one-sided fiber growth in this section is a result on the noncoaxiality in the XZ section [Etchecopar and Malavielle, 1987]. Sample locations are shown in Figure 3, and cumulative incremental and progressive finite strain history curves are shown in Figure 5. These curves show a consistent sense of rotation of the extension direction from negative to positive angles (i.e., a counterclockwise rotation). Also, for three of the four samples, the progressive finite strain curve ends parallel to cleavage ($\Theta = 0^\circ$), indicating that the finite strain ellipse is parallel to cleavage. This observation strongly suggests that the noncoaxial strain is contemporaneous with cleavage formation.

KINEMATIC MODELS

In this section, we develop a kinematic model for the Hsüehshan Range by integrating incremental strain data with field observations. Then we use Dahlen and Barr's [1989] kinematic model to quantitatively predict the strain magnitudes at the surface of the wedge.

Kinematic Model Based on Incremental Strain Data

Incremental strain data indicate that much of the eastern Hsüehshan Range is characterized by coaxial strain histories, regardless of position on minor folds. This observation is in contrast to folding models [Beutner and Diegel, 1985; Wickham and Anthony, 1977] in which opposing limbs of a fold may experience different strain histories. Because the strain histories are coaxial within regions I and II, folding is attributed in part to passive rotation of bedding due to penetrative coaxial strain with updip extension (i.e., bedding rotated as a passive line marker).

Elongations of the order of 1.5 to 2.5, however, are insufficient to account for the $\sim 80^\circ$ - 90° of rotation required to rotate bedding into near parallelism with cleavage, both of

central fiber is straight, and the pressure shadow tapers in width away from the pyrite, suggesting that the pressure shadow is deformable and shortened parallel to Z. (c) Photomicrograph of a pressure shadow from sample 90-88 (XZ section, viewed toward the northeast), indicating a noncoaxial strain history. Cleavage is approximately vertical in the outcrop. Because fiber growth is antitaxial, the curvature of the fibers is consistent with a component of top-to-the-east simple shear.

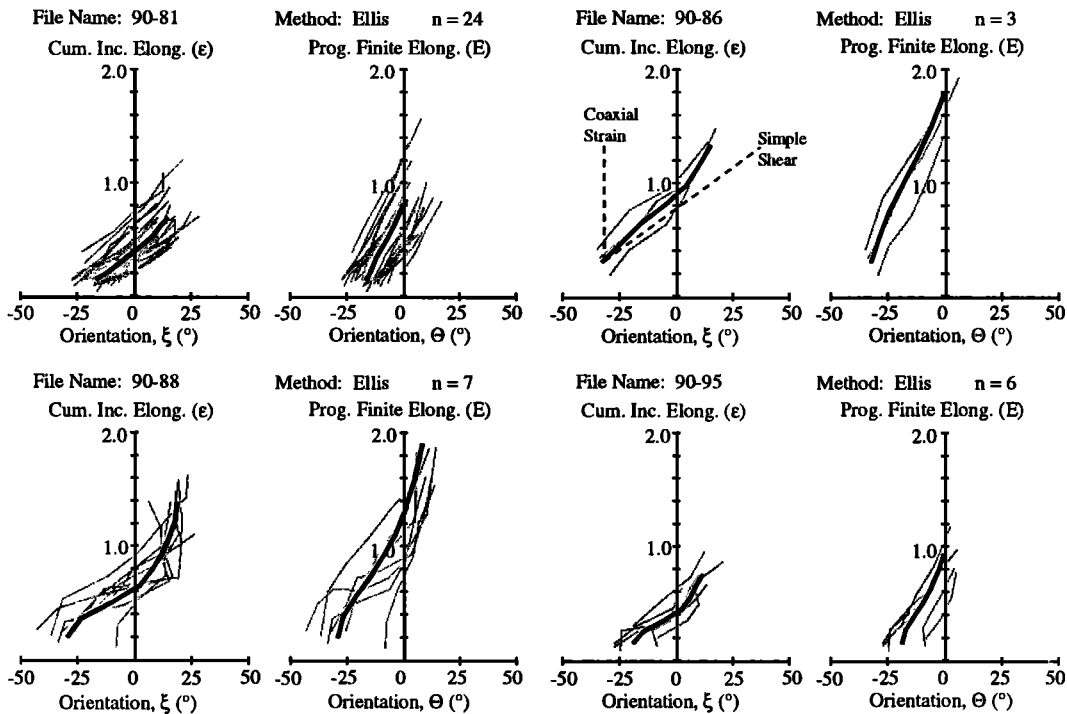


Fig. 5. Cumulative incremental strain history and progressive finite strain diagrams for samples with noncoaxial strain histories. The orientation is measured relative to cleavage, where positive angles are counterclockwise. The gray curves represent the strain histories recorded by individual fibers from a single sample; the black curve represents an average strain history for that sample. The sample locations are shown in Figure 3.

which are subvertical in the slates. Significant rotation of bedding not recorded by fibrous overgrowths is required to account for much of this of rotation. Although the Tachien anticline is interpreted to have formed as a result of buckling,

incremental strain histories are coaxial in slate interbeds on the southeast limb. We suggest that folding occurred as a result of buckling of the relatively stiff Tachien Sandstone but that buckling was not accompanied by significant penetrative

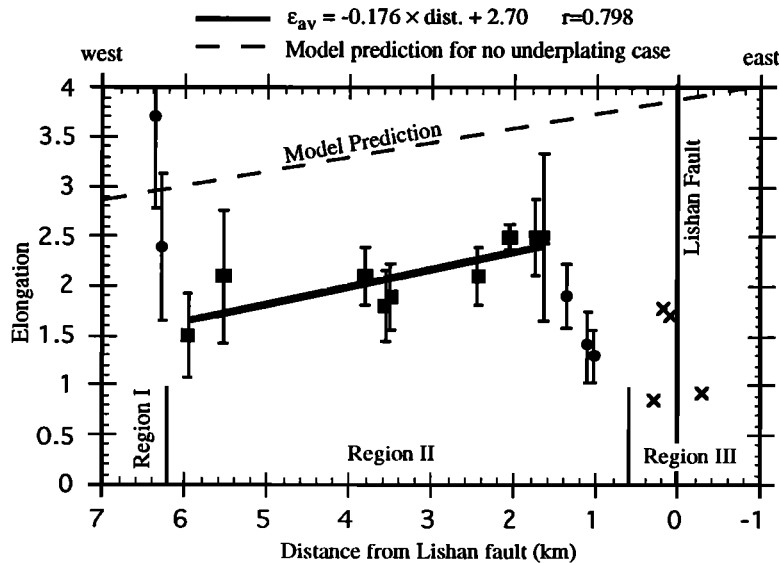


Fig. 6. Plot of elongation versus distance from the Lishan fault, where the solid squares and circles represent the average measured elongations from samples with coaxial strain histories, and crosses represent the maximum finite elongations measured in samples with noncoaxial strain histories. Error bars show one standard deviation. The solid squares show a progressive increase in strain magnitude toward the hinterland, shown by the solid black line. The dashed curve (nonlinear) shows the elongations predicted at the surface by the Dahlen and Barr [1989] no underplating model.

deformation as recorded by pressure shadows. This interpretation is similar to an observation by Beutner [1978] in the Martinsburg Slate where folding was accommodated predominantly by flexural slip during buckling of sandstone interbeds (for limb dips between -10° – -50°) but with the absence of significant cleavage-forming strain. Penetrative strain recorded by pressure shadows resulted in further steepening of bedding in the Chiayang Formation, as bedding rotated passively into near parallelism with cleavage.

Near the Lishan fault in region III, incremental strain histories are noncoaxial and have a sense of curvature that may reflect (1) a clockwise rotation of the rock through a constant extension direction, (2) a counterclockwise rotation of the extension direction relative to the rock, or (3) a component of clockwise simple shear (Figure 5). If these rocks had experienced a clockwise rotation of 30° – 45° (Figure 5), it is expected that cleavage and bedding would dip 45° – 60° toward the northwest. In the vicinity of the Lishan fault, cleavage and bedding are oriented approximately the same as elsewhere in the Chiayang Formation, so rotation of the rock through a constant extension direction is ruled out.

Although rotation of the extension direction relative to the rock cannot strictly be ruled out, a more likely explanation is that fiber curvature is related to a component of top-to-the-east simple shear near the boundary between the Hsüehshan and Backbone ranges, a known fault contact. Assuming that the youngest fibers are at an angle of 45° to the shear zone boundaries, the shear zone dips steeply to the NW, and therefore the Lishan fault is a SE-vergent backthrust. The older, higher-grade rocks of the Hsüehshan Range are thrust to the SE over the younger, lower-grade rocks of the western Backbone Range (Figure 7). This interpretation differs from previous interpretations [Biq, 1971] which suggest that the Lishan fault is a SE dipping, NW-vergent thrust, but the orientation is consistent with the suggestion by Teng et al. [1991] that the Lishan fault may initially have developed as a west dipping growth fault. Syncleavage deformation may have reactivated this preexisting normal fault during collision and inversion of the passive margin. The Hsüehshan Range is therefore a pop-up structure bounded to the west by the NW-vergent Chüchih fault and to the east by the SE-vergent Lishan fault (Figure 7).

The total amount of rotation determined from the stacked curves ranges from $\xi = 31^{\circ}$ to 47° , and the cumulative incremental strains range from $\epsilon = 0.7$ to 1.3. The resulting

gradient, $d\xi/de$, ranges from $3.4^{\circ}/0.1$ to $4.5^{\circ}/0.1$. This gradient is lower than that for simple shear ($5.7^{\circ}/0.1$) [Gray and Durney, 1979], suggesting there are components of both simple shear and pure shear in the vicinity of the Lishan fault.

Because the Lishan fault is not exposed in the vicinity of the Central Cross-Island Highway, we use the locations of samples with noncoaxial strain histories as well as the approximate location of the contact between the Chiayang and Lushan formations to locate the fault on the map (Figure 1). Whereas samples 90-81, 90-86, and 90-88 contain no fossils and are identified as Chiayang Formation, sample 90-95 contains abundant fossils and shows some amount of radial extension in XY sections, observations which are typical of the Lushan Formation [J. Crespi, personal communication, 1991]. Thus samples 90-81, 90-86, and 90-88 are from the Chiayang Formation in the hanging wall of the Lishan fault, and sample 90-95 is from the Lushan Formation in the footwall. This interpretation is consistent with geologic observations as it suggests that the higher-grade, Eo-Oligocene rocks of the Chiayang Formation in the hanging wall are thrust over the lower-grade, Miocene rocks of the Lushan Formation in the footwall.

Theoretical Models for Wedge Kinematics

Dahlen and Barr [1989] develop a steady state kinematic model for an isotropic, wedge-shaped mountain belt where material within the wedge experiences subhorizontal shortening and subvertical extension. Particles enter the wedge by accretion at the toe and underplating along the base and follow hyperbolic paths through the wedge until they are removed by erosion at the surface. The wedge geometry and coordinate axes are shown in Figure 8. Velocities within the wedge are a function only of the wedge geometry and the rates of accretion, underplating, and erosion at the boundaries. These models assume that (1) the material within the wedge is incompressible, (2) the principal strain rates are parallel to the principal stress directions (isotropic), and (3) there is no along strike extension. The plane strain assumption (assumption 3) is consistent with observations from the eastern Hsüehshan Range, where pressure shadows suggest that the rocks experienced no shortening or extension parallel to Y.

The Eulerian velocities, $\mathbf{u} = u\hat{x} + v\hat{z}$, are predicted by the model, and the principal strain rates are given by Dahlen and Barr [1989] as

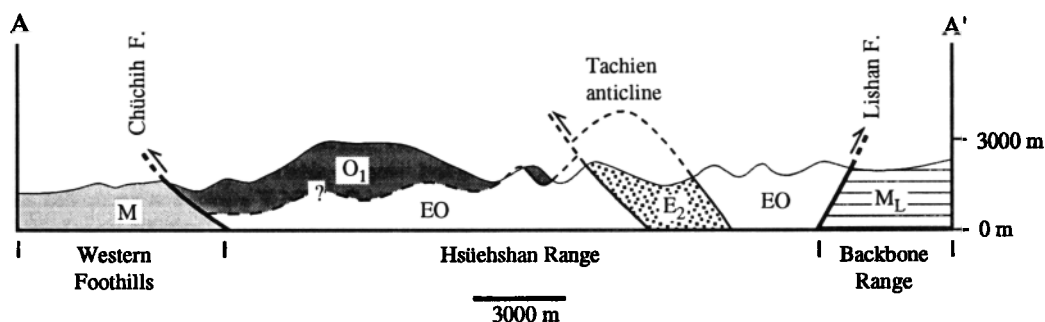


Figure 7. Schematic cross section through the Hsüehshan Range showing the major structural and stratigraphic contacts. The Hsüehshan Range is bounded to the west by the NW-vergent Chüchih fault and to the east by the SE-vergent Lishan fault; thus the Hsüehshan Range is envisaged as a pop-up structure flanked to either side by younger, lower-grade rocks. The location of the cross section is shown in Figure 2.

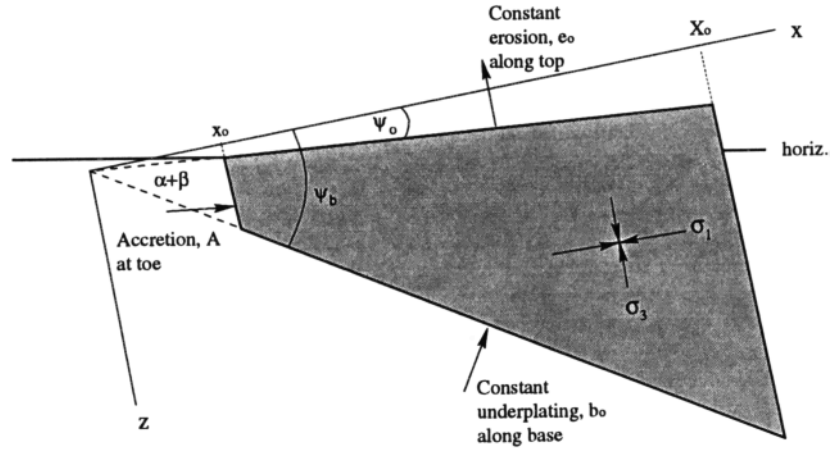


Figure 8. Schematic cross section of a wedge-shaped mountain belt showing the coordinate system and variables used in the Dahlen and Barr [1989] kinematic model. Redrawn from Dahlen and Barr [1989].

$$\dot{\epsilon}_1 = \frac{\partial u}{\partial x} \quad \dot{\epsilon}_3 = \frac{\partial v}{\partial z} \quad (3)$$

where

$$\dot{\epsilon}_1 = -\dot{\epsilon}_3 = B - Cx^{-2} \left(1 + \frac{z^2}{x^2} \right) \left(1 - \frac{z^2}{x^2} \right)^{-2}, \quad (4)$$

and

$$B = \frac{-E \sin \alpha}{\sin 2\psi_b - \sin 2\psi_0}, \quad (5)$$

$$C = \frac{2\dot{A} + 2x_0(\dot{e}_0 \sec \psi_0 - \dot{b}_0 \sec \psi_0) + E(x_0^2 \sin \alpha \sec^2 \psi_0)}{\log \left[\frac{(1 + \tan \psi_b)(1 - \tan \psi_0)}{(1 - \tan \psi_b)(1 + \tan \psi_0)} \right]}. \quad (6)$$

All variables are defined in Table 2. The pure rotation rate component of the deformation is given by

$$\frac{\dot{\Omega}}{2} = \frac{1}{2} \left(\frac{\partial u}{\partial z} - \frac{\partial v}{\partial x} \right) = \frac{Cz}{x^3 \left(1 - \frac{z^2}{x^2} \right)^2} + \frac{Cz^3}{x^5 \left(1 - \frac{z^2}{x^2} \right)^2} + \frac{Cz}{x^3 \left(1 - \frac{z^2}{x^2} \right)} - B \sin \psi_b. \quad (7)$$

Knowing the strain rates and rotation rates at every point within the wedge, it is possible to calculate the cumulative amount of strain a rock at the surface should have experienced while deforming within the wedge by integrating the strain rate with respect to time over a complete particle path. This can be done numerically using a finite difference approach and treating each increment of strain as a pure strain followed by a pure rotation. The pure strain component for each increment

is represented by the matrix

$$\begin{bmatrix} (\dot{\epsilon}_1 \Delta t + 1) & 0 \\ 0 & (\dot{\epsilon}_1 \Delta t + 1)^{-1} \end{bmatrix}_i, \quad (8)$$

and the rigid rotation is $\omega_i = 0.5 \dot{\Omega}_i \Delta t$, where the subscript i refers to an increment of strain. To calculate the finite strains, each incremental stretch tensor must be transformed into a common reference frame. For convenience, we have chosen an external reference frame parallel to the principal stress directions. The incremental stretch tensors in the external reference frame are given by

$$\begin{bmatrix} \sqrt{\lambda_{11}} & \sqrt{\lambda_{12}} \\ \sqrt{\lambda_{21}} & \sqrt{\lambda_{22}} \end{bmatrix}_i = \quad (9)$$

$$\begin{bmatrix} \cos \omega_i & -\sin \omega_i \\ \sin \omega_i & \cos \omega_i \end{bmatrix} \begin{bmatrix} \sqrt{\lambda_1} & 0 \\ 0 & \sqrt{\lambda_2} \end{bmatrix}_i \begin{bmatrix} \cos \omega_i & \sin \omega_i \\ -\sin \omega_i & \cos \omega_i \end{bmatrix}$$

The finite stretch tensor is then determined by multiplication of the incremental stretch tensors [Wickham, 1977]

$$\begin{bmatrix} a & b \\ c & d \end{bmatrix}_f = \begin{bmatrix} a & b \\ c & d \end{bmatrix}_n \dots \begin{bmatrix} a & b \\ c & d \end{bmatrix}_2 \begin{bmatrix} a & b \\ c & d \end{bmatrix}_1, \quad (10)$$

where a , b , c , and d are entries in the stretch tensor. The subscripts 1, 2, ..., n serve to distinguish strain increments and f refers to the finite stretch tensor.

Maintaining a constant wedge geometry, the velocities and rock trajectories within the wedge can be affected by changing the rates of accretion, underplating, and erosion, as long as the net flux is equal to zero. Strain calculations were performed for three cases, including no underplating, 25% underplating, and 50% underplating. The results are shown in Figure 9. Whereas finite strains increase progressively across the entire wedge for the no underplating case, finite strains increase then decrease toward the hinterland in the 25% and 50% underplating cases. This decrease occurs because underplated rocks bypass the toe of the wedge where strain rates are

TABLE 2. List of Variables and Corresponding Values Used to Calculate the Principal Stretches Predicted by the Dahlen and Barr [1989] Kinematic Model

Variable	Parameter	Value (Comment)
x, z	coordinates in principal stress parallel coordinate system	km
ϵ_1, ϵ_3	maximum and minimum principal elongations	
$\dot{\epsilon}_1, \dot{\epsilon}_3$	maximum and minimum principal strain rates	m.y. ⁻¹
\dot{A}	accretionary influx rate at the toe	500 km ² m.y. ⁻¹ (no underplating)* 334 km ² m.y. ⁻¹ (25% underplating)* 250 km ² m.y. ⁻¹ (50% underplating)*
\dot{b}_0	underplating rate, constant along entire base	0.0 km m.y. ⁻¹ (no underplating)* 1.8 km m.y. ⁻¹ (25% underplating)* 2.7 km m.y. ⁻¹ (50% underplating)*
$\dot{\epsilon}_0$	erosion rate along entire top	5.5 km m.y. ⁻¹ (all cases)*
E	linear erosion coefficient (used to simulate an erosion rate which increases with elevation)	0.0 (not used)*
x_0	distance to deformation front	45 km*
α	surface taper of wedge	3°*
ψ_0	surface stress orientation	4°*
ψ_b	basal stress orientation	13°*
$\dot{\Omega} / 2$	pure rotation rate component of deformation	radians m.y. ⁻¹
ω	pure rotation component of deformation	radians
Δt	time step for numerical integration	0.0005 m.y.

*Values as defined by Barr and Dahlen [1989].

highest [Dahlen and Barr, 1989]. For example, a particle that reaches the surface of the wedge at the point B (Figure 9) enters the toe of the wedge at point A in the no underplating case (Figure 9a), point A' in the 25% underplating case (Figure 9b), and point A'' in the 50% underplating case (Figure 9c).

COMPARISON OF KINEMATIC DATA WITH MODEL PREDICTIONS

Kinematic data determined from field and microstructural observations within the eastern Hsüehshan Range indicate that (1) the extension direction is updip and parallel to the steep, southeast dipping cleavage, (2) strain magnitudes generally increase toward the hinterland, and pressure shadows record coaxial strain histories throughout much of the region, and (3) region III, near the Lishan fault, is characterized by noncoaxial strain histories consistent with a top-to-the-east sense of shear.

Southeast Dipping Cleavage and Up-Dip Extension

In Dahlen and Barr's [1989] kinematic model, the orientation of the principal axes of the finite strain ellipse reflects both the pure strain and pure rotation components of the deformation. Considering only the pure strain component, the principal shortening direction will be parallel to the maximum principal stress direction (isotropic material), which plunges to the NW at an angle of $\psi_0 + \alpha = 7^\circ$. The pure rotation component results in a counterclockwise rotation of the finite strain ellipse by an amount that increases from west

to east across the wedge. In the vicinity of the eastern Hsüehshan Range, the total rotation of the finite strain ellipse predicted by the no underplating model is on the order of $5^\circ - 5.5^\circ$ (Figure 9). Cleavage in this region should therefore dip $\sim 78^\circ$ to the SE and the extension direction should plunge to the SE $\sim 78^\circ$. These predictions conform quite well with field observations where cleavage generally dips steeply to the SE between 75° and 80° (Figure 3.c) and the stretching lineation plunges to the SE between 75° and 80° (Figure 3.d).

Comparison of Measured and Predicted Strain Magnitudes

With the exception of slate interbeds within the Tachien Sandstone and rocks from near the Lishan fault, pressure shadows show a progressive increase in finite strain magnitude from west to east across the field area. Figure 6 shows a plot of elongation versus distance from the Lishan fault. Although the Dahlen and Barr [1989] no underplating model predicts a similar increase in finite strain magnitude toward the hinterland (dashed line), the model predictions are slightly higher than elongations measured from pyrite pressure shadows. The discrepancy between the predicted and measured values may reflect (1) volume-loss strain or (2) strain localization along discrete shear zones (e.g., the Lishan fault).

Volume-loss strain of the order of up to approximately 50% has previously been recognized in slate terranes such as the Martinsburg Formation [Wright and Platt, 1982] and the Hamburg sequence [Beutner and Charles, 1985]. Beutner and

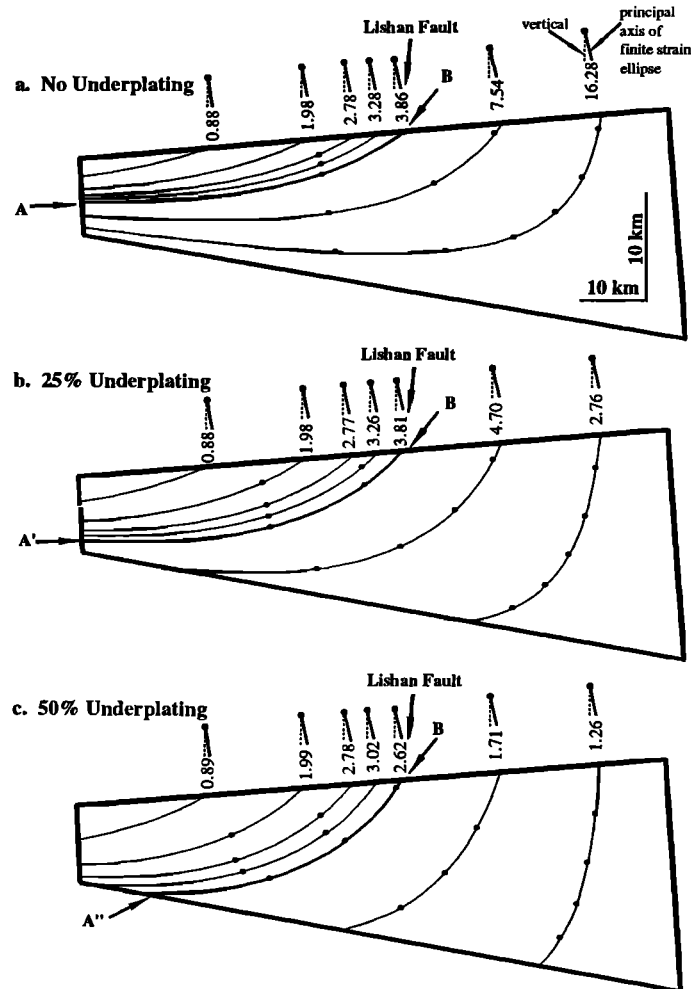


Figure 9. Diagrams showing the particle paths and elongations predicted Dahlen and Barr's [1989] kinematic model for three cases, including (a) no underplating, (b) 25% underplating, and (c) 50% underplating. Dots represent 1 m.y. time intervals. The points A, A', and A'' show the entry points for a particle which eventually exits at point B. The location of the Lishan fault is shown by the arrow; the field area extends approximately 12 km west of the fault.

Charles [1985], however, suggest that in slates where volume loss has played an important role, fibrous overgrowths are insignificant or absent. In slates from the eastern Hsüehshan Range, pressure shadows are common and relatively long, suggesting that volume loss probably did not play an important role.

Although volume-loss strain cannot strictly be ruled out, we feel that significant deformation is accommodated along relatively narrow shear zones. At the scale of a thin section, the presence of a well-developed cleavage defined by an insoluble residue as well as fibrous overgrowths adjacent to biotite, pyrite, and quartz grains suggest that diffusive mass transfer is the dominant deformation mechanism. Nevertheless, at the scale of the slate belt, numerous faults have been mapped (e.g., the Lishan fault), suggesting that a significant portion of the bulk strain may be accommodated along faults. Because part of the bulk strain is being accommodated along discrete shear zones, it is expected that the model would predict higher penetrative strain than that experienced by an unfaulted rock volume within the wedge.

Although samples 90-81, 90-86, 90-88, and 90-95 record finite strains similar in magnitude to nearby rocks with coaxial strain histories, it is important to note that these samples are from the hanging wall and footwall of the Lishan fault and therefore do not record all of the shortening accommodated across the fault itself. We infer that significant strain is accommodated across the Lishan fault to account for the displacement necessary to emplace lower greenschist facies rocks adjacent to prehnite-pumpellyite grade rocks but that not all of the shortening is recorded by pressure shadows.

CONCLUSIONS

On the bases that (1) the Lishan fault juxtaposes the greenschist facies Eo-Oligocene rocks of the Hsüehshan Range against the prehnite-pumpellyite grade Miocene rocks of the western Backbone Range and (2) the incremental strain histories from near this contact are consistent with a top-to-the east sense of shear, the Lishan fault is interpreted to be a major, west dipping backthrust. Given that the western

boundary of the Hsüehshan Range is the east vergent Chüchih fault and the eastern boundary is the east vergent backthrust, the Hsüehshan Range is envisaged as a large-scale pop-up structure. The Hsüehshan Range is therefore an anticlinorium cored by biotite grade rocks. This anticlinorium exposes higher-grade Eo-Oligocene rocks in the center of the Taiwan mountain belt and is flanked on either side by lower-grade Miocene rocks. In southern Taiwan, the Hsüehshan Range tapers in width and is interpreted to lie beneath the Miocene thrust sheets of the Backbone Range [Chen and Chuang, 1989]. Where the Hsüehshan Range is not exposed (e.g., southern Taiwan), ages increase progressively across the mountain belt from Plio-Pleistocene in the Western Foothills to Mesozoic in the pre-Tertiary metamorphic complex. Thus the pop-up structure may be buried or die out to the south where the collision is younger.

The presence of this fault-bounded pop-up which exposes higher-grade, Eo-Oligocene rocks in the middle of the mountain belt differs significantly from wedge models which treat the mountain belt as isotropic because these models predict a progressive increase in age and metamorphic grade from foreland to hinterland. Deformation at the scale of the mountain belt is both heterogeneous and anisotropic, suggesting that the pre-tectonic passive margin stratigraphy and

preexisting normal faults play an important role in the structural evolution of Taiwan. For example, the early stages of folding are characterized by the buckling of the relatively stiff Tachien Sandstone. Moreover, shortening associated with the arc-continent collision was concentrated along the Lishan fault, reflecting an inversion of a major extensional structure [Teng et al., 1991] related to earlier rifting.

Acknowledgments. Thanks to reviewers D. Anastasio and R. Dorsey whose comments significantly improved this paper. We would like to thank T. Byrne, J. Crespi, and K. Tillman for helpful discussions in the field and M. Brandon for discussions about the kinematic models. We would also like to thank everyone at National Taiwan University and at the Central Geological Survey of Taiwan, including, among others, L. Teng, C.K. Fong, K.-S. Shea, T.-K. Liu, C.-H. Chen, Y.-C. Chan, and T.-L. Chang, who helped us both scientifically and logistically. Support for this project was provided by a grant to D.F. from the National Science Foundation (EAR-8904989), as well as by a P.D. Krynine Research Grant (to B.C.) from Pennsylvania State University. Field transportation was provided by the Central Geological Survey. Thanks to R. Allmendinger for the use of "Stereonet".

REFERENCES

- Barr, T.D., and F.A. Dahlen, Brittle frictional mountain building, 2, Thermal structure and heat budget, *J. Geophys. Res.*, 94, 3923-3947, 1989.
- Barr, T.D., F.A. Dahlen, and D.C. McPhail, Brittle frictional mountain building, 3, Low-grade metamorphism, *J. Geophys. Res.*, 96, 10,319-10,338, 1991.
- Beutner, E.C., Slaty cleavage and related strain in Martinsburg Slate, Delaware Water Gap, New Jersey, *Am. J. Sci.*, 278, 1-23, 1978.
- Beutner, E.C., and E.G. Charles, Large volume loss during cleavage formation, Hamburg sequence, Pennsylvania, *Geology*, 13, 803-805, 1985.
- Beutner, E.C., and F.A. Diegel, Determination of fold kinematics from syntectonic fibers in pressure shadows, Martinsburg slate, N.J., *Am. J. Sci.*, 285, 16-50, 1985.
- Big, C.C., Some aspects of post-orogenic block tectonics in Taiwan. Recent crustal movements, *Bull. R. Soc. N. Z.*, 9, 19-24, 1971.
- Chen, C.-H., Geology of the east-west cross-land highway in central Taiwan, *Mem. Geol. Soc. China*, 3, 219-236, 1979.
- Chen, C.-H., Change of X-ray diffraction pattern of K-micas in the metapelites of Taiwan and its implication for metamorphic grade, *Mem. Geol. Soc. China*, 4, 475-490, 1981.
- Chen, C.-H., Determination of lower greenschist facies boundary by K-mica -- chlorite crystallinity in the Central Range, Taiwan, *Proc. Geol. Soc. China*, 27, 41-53, 1984.
- Chen, C.H., and T.Y. Chuang, Geology of the southwest Central Range and a structural interpretation of the Central Range of Taiwan (in Chinese with English abstract), *Bull.*, 5, pp. 1-18, Cent. Geol. Surv., Taipei, 1989.
- Chen, C.H., H.T. Chu, H.G. Liou, and W.G. Ernst, Explanatory notes for the metamorphic facies map of Taiwan, Spec. Publ. 2, 32 pp., Cent. Geol. Surv., Taipei, 1983.
- Crespi, J., Structural patterns in a belt of anomalously low-grade rocks in the hinterland of the Taiwan arc-continent collision, *Eos Trans. AGU*, 72, Fall Meeting Suppl., p. 432, 1991.
- Dahlen, F.A., and T.D. Barr, Brittle frictional mountain building, 1, Deformation and mechanical energy budget, *J. Geophys. Res.*, 94, 3906-3922, 1989.
- Durney, D.W., and J.G. Ramsay, Incremental strains measured by syntectonic crystal growths, in *Gravity and Tectonics*, edited by K. DeJong and R. Sholten, pp. 67-96, John Wiley, New York, 1973.
- Ellis, M., The determination of progressive deformation histories from antitaxial syntectonic crystal fibres, *J. Struct. Geol.*, 8, 701-709, 1986.
- Etchecopar, A., and J. Malavieille, Computer models of pressure shadows: a method for strain measurement and shear-sense determination, *J. Struct. Geol.*, 9, 667-677, 1987.
- Fisher, D.M., Orientation history and rheology in slates, Kodiak and Afognak Islands, Alaska, *J. Struct. Geol.*, 12, 483-498, 1990.
- Fisher, D.M., and T. Byrne, Strain variations in an ancient accretionary complex: Implications for orogenic evolution, *Tectonics*, 11, 330-347, 1992.
- Gray, D.R., and D.W. Durney, Investigations on the mechanical significance of crenulation cleavage, *Tectonophysics*, 58, 35-79, 1979.
- Ho, C.S., *An Introduction to the Geology of Taiwan—Explanatory Text of the Geologic Map of Taiwan*, 153 pp., Ministry of Economic Affairs, Taipei, Taiwan, Republic of China, 1975.
- Ho, C.S., A synthesis of the geologic evolution of Taiwan, *Tectonophysics*, 125, 1-16, 1986.
- Ho, C.S., *An Introduction to the Geology of Taiwan—Explanatory Text of the Geologic Map of Taiwan*, 2nd ed., 192 pp., Ministry of Economic Affairs, Taipei, Taiwan, Republic of China, 1988.
- Hsieh, X.-L., Fission-track dating of zircons from several east-west cross sections of Taiwan island, unpublished M.S. thesis, National Taiwan Univ., Taipei, 1990.
- Lee, C.R., and W.T. Cheng, Preliminary heat flow measurements in Taiwan, *Proceedings of the Fourth Circum-Pacific Energy and Mineral Resources Conference*, Singapore, 1986.
- Liu, T.-K., Tectonic implication of fission track ages from the Central Range, Taiwan, *Proc. Geol. Soc. China*, 25, 22-37, 1982.
- Liu, T.-K., Fission track dating of the Hsüehshan Range: Thermal record due to arc-continent collision in Taiwan, *Acta Geologica Taitungica*, 26, 279-290, 1988.
- Lundberg, N., and R.J. Dorsey, Synorogenic sedimentation and subsidence in a Plio-Pleistocene collisional basin, eastern Taiwan, in *New Perspectives in Basin Analysis*, edited by K. L. Kleinspenn and C. Paola, pp. 265-280, Springer-Verlag, New York, 1988.
- Ramsay, J.G., and M.I. Huber, *The Techniques of Modern Structural Geology*, vol. 1, *Strain Analysis*, Academic, San Diego, Calif., 1983.
- Seno, T., The instantaneous rotation vector of the Philippine Sea plate relative to the Eurasian plate, *Tectonophysics*, 42, 209-226, 1977.
- Suppe, J., A retrodeformable section of northern Taiwan, *Proc. Geol. Soc. China*, 23, 46-55, 1980.
- Suppe, J., Mechanics of mountain building and metamorphism in Taiwan, *Mem. Geol. Soc. China*, 4, 67-89, 1981.
- Teng, L.S., Y. Wang, C.-H. Tang, C.-Y. Huang, T.-C. Huang, M.-S. Yu, and A. Ke, Tectonic aspects of the Oligocene depositional basin of northern Taiwan, *Proc. Geol. Soc. China*, 34, 313-336, 1991.
- Tillman, K.S., T. Byrne, C.-Y. Lu, and C.-H. Chen, Strain partitioning in the foreland to hinterland transition: Hsüehshan Range, Taiwan, R.O.C., *Geol. Soc. Am. Abstr. Programs*, 23, 423, 1991.
- Wickham, J.S., An estimate of strain increments in a naturally deformed carbonate rock, *Am. J. Sci.*, 273, 23-47, 1973.
- Wickham, J.S., and M. Anthony, Strain paths and folding of carbonate rocks near Blue Ridge, central Appalachians, *Geol. Soc. Am. Bull.*, 88, 920-924, 1977.
- Wright, T.O., and L.G. Platt, Pressure dissolution and cleavage in the Martinsburg Shale, *Am. J. Sci.*, 282, 122-135, 1982.
- Wu, F.T., Recent tectonics of Taiwan, *J. Phys. Earth*, 26, S265-S299, 1978.
- Yen, T.P., The Eocene sandstones in the Hsüehshan Range terrain, northern Taiwan, *Proc. Geol. Soc. China*, 16, 97-110, 1973.
- C.-H. Chen, Central Geological Survey, M.O.E.A., Taipei, Taiwan, R.O.C.
- M. B. Clark and D.M. Fisher, Department of Geosciences, Pennsylvania State University, University Park, PA 16802.
- C.-Y. Lu, Department of Geology, 245 Choushan Rd. National Taiwan University, Taipei, Taiwan, R.O.C.

(Received December 24, 1991;
revised July 9, 1992;
accepted July 21, 1992.)